Acta Cryst. (1979). A35, 511–524

The Calculation and Interpretation of High-Resolution Electron Microscope Images of Lattice Defects

BY G. R. ANSTIS AND D. J. H. COCKAYNE

Electron Microscope Unit, University of Sydney, NSW, 2006, Australia

(*Received* 24 *October* 1978; *accepted* 29 *January* 1979)

Abstract

Limitations on the calculation of high-resolution detail in electron microscope images of defects in crystals are discussed and it is shown how images of crystals with arbitrary strain can be calculated by means of a reinterpretation of the normal dynamical equations. An alternative approach, which in some cases is preferable for numerical calculations, is the method of periodic continuation. These methods, and various approximations to them, are applied to the study of high-resolution images of edge dislocations. It is shown that at the 5 Å level of resolution, the column approximation is adequate for calculating the important features of weak-beam images of an edge dislocation with an extended core. However, when applied to the calculation of lattice fringes near a core, it may lead to serious error. Calculations are presented which show that, because of spherical aberration, care is required in the interpretation of lattice-fringe images near a dislocation core even for thin crystals.

1. Introduction

High-resolution electron microscope studies of lattice defects require accurate image computation for establishing the range of validity of detailed image interpretation. Two approaches for computing images have been developed in the literature, one being to approximate the imperfect crystal by an artificially periodic structure and to perform the calculation as for a perfect crystal, and the other being to calculate the scattering for a series of columns in the direction of the incident electron beam. Estimates of the limits of resolution, beyond which approximations based on the latter approach are suspect, have appeared in the literature, but no rigorous determination of their range of validity has been given. This has resulted in confusion as to when this approach can be employed.

In this paper the relationship between the various methods of computation is investigated, and the limitations and interpretation of a number of approximations and models discussed. These investigations are used to study the interpretation of high-resolution lattice-fringe and weak-beam images of dislocations.

2. The theory of diffraction in an imperfect crystal

A number of approximations have been developed to describe mathematically the diffraction by, and imaging of, crystals containing defects. The work of Hirsch, Howie & Whelan (1960), Howie & Whelan (1961, 1962) and Wilkens (1966) involve applications of the column approximation. Takagi (1962) and Jouffrey & Taupin (1967) consider an extension to this approximation whereby images of higher resolution and regions of increasing lattice distortion can be considered. A more general scattering equation is discussed by Howie & Basinski (1968) who conclude that it is adequate for all but the most severely-distorted crystals. We shall refer to these analyses as the direct-space approach since the equations involve functions of position.

An alternative approach has been considered by Grinton & Cowley (1971) who approximate the problem of scattering by a single defect to one involving a periodic lattice, each unit cell of which consists of a portion of the deformed crystal containing the single defect. The problem then becomes one of considering a perfect crystal, albeit with a large unit cell. In addition to the Bragg beams of the original perfect-crystal lattice, Bragg beams of the artificially periodic lattice are also considered. These correspond in position to diffuse scattering in the diffraction pattern of the perfect crystal. This method, which is most convenient for calculations in reciprocal space, is known as the method of periodic continuation.

In this section it is shown how the direct-space approach and the method of periodic continuation are related. In the course of the analysis it will be shown that the set of direct space equations considered by Howie & Basinski (1968) is valid *irrespective of the degree of distortion of the crystal*, but that its use in the calculation of image intensities is cumbersome when the crystal is highly distorted. We also discuss the column approximation, the validity of which is shown to

0567-7394/79/040511-14$01.00

depend upon the distribution of diffuse scattering about the Bragg reflection, upon the wavelength of the electrons and upon the thickness of the crystal.

2.1. *Derivation of the equations of direct space*

In order to derive the set of equations in direct space mentioned above, we begin with that form of Schrödinger's equation in which back-scattering is neglected (Tournarie, 1962; Goodman & Moodie, 1974). Defining the z axis to be normal to the entrance face of the crystal which is the plane $z = 0$, with $\Psi(\mathbf{r})$ the wavefunction of the electron travelling approximately in the positive z direction and $v(\mathbf{r})$ the crystal potential, it can be shown that the wavefunction $\psi \equiv \psi(\mathbf{r}) = \Psi(\mathbf{r})\exp(-i\mathbf{k}.\mathbf{r})$ satisfies (to a good approximation for electrons of moderately high energies) the equation

$$\frac{\partial\psi}{\partial z} = \frac{i}{2k_z}\left[\frac{\partial^2\psi}{\partial x^2} + \frac{\partial^2\psi}{\partial y^2} + 2ik_x\frac{\partial\psi}{\partial x} + 2ik_y\frac{\partial\psi}{\partial y}\right] + i\sigma v(\mathbf{r})\psi, \tag{2.1}$$

where $\mathbf{k}$ is a wavevector with components k_x, k_y, k_z and magnitude $k = 2\pi/\lambda$, λ being the wavelength of the electrons, σ is the interaction constant given by

$$\sigma = \frac{me}{\hbar^2 k_z}. \tag{2.2}$$

In deriving equation (2.1) from Tournarie's equation, the Fresnel approximation for wave propagation is made and terms containing the factor $\lambda\sigma$ are considered negligible. The incident wavefunction must be consistent with the assumption that scattering in the negative z direction is negligible, but it need not be planar. Equation (2.1) can be applied to a choice of initial wavefunctions appropriate for calculating microdiffraction intensities and convergent beam patterns obtained by using a coherent source of electrons, as well as for the more straightforward situation of parallel illumination.

Equation (2.1) may be used to calculate images and diffraction patterns of an imperfect crystal, but the occurrence of the second derivatives of the wavefunction causes computational difficulties except for very thin crystals. However, a more manageable set of equations can be developed to replace the single equation (2.1) by expanding the potential $v(\mathbf{r})$ in the series

$$v(\mathbf{r}) = \sum_{\mathbf{g}} u_{\mathbf{g}}(\mathbf{r})\exp(2\pi i\mathbf{g}.\mathbf{r}). \tag{2.3}$$

In principle, the vectors $\mathbf{g}$ may be any set of vectors in reciprocal space, but generally a useful choice, if the crystal is not too distorted, is a set of reciprocal-lattice vectors corresponding to the perfect crystal which lie in a plane approximately perpendicular to the z axis. The functions $u_{\mathbf{g}}(\mathbf{r})$ are also arbitrary but two convenient choices will be mentioned (see also § 4.2). The first, applicable under the deformable-ion model (for which $v_d(\mathbf{r}) = v_p[\mathbf{r} - \mathbf{R}(\mathbf{r})]$, where $v_p(\mathbf{r})$ and $v_d(\mathbf{r})$ are the potentials of the perfect and imperfect crystals respectively, and where $\mathbf{R}(\mathbf{r})$ is the displacement field associated with the defect), is

$$u_{\mathbf{g}}(\mathbf{r}) = V_{\mathbf{g}}\exp[-2\pi i\mathbf{g}.\mathbf{R}(\mathbf{r})], \tag{2.4}$$

where $V_{\mathbf{g}}$ is a Fourier coefficient of the potential of the perfect crystal. A second choice is to define $u_{\mathbf{g}}(\mathbf{r})$ so that it has Fourier components corresponding to wavevectors only in the first Brillouin zone and, if $\mathbf{u}$ is such a wavevector, its Fourier transform at $\mathbf{u}$ equals the Fourier transform of $v(\mathbf{r})$ evaluated at $\mathbf{g} + \mathbf{u}$. This is the choice made when the rigid-ion model for the potential is used. For this model the potential in the crystal lattice equals the sum of the potentials of each atom in the distorted crystal. The potential due to one atom is assumed equal to its potential in the perfect crystal. The effect upon image calculations of choosing between these two approximations is considered in § 4.

Having chosen a set of functions $u_{\mathbf{g}}(\mathbf{r})$, we define the functions $\varphi_{\mathbf{g}}(\mathbf{r})$ by requiring that they satisfy the two conditions

$$\psi(x,y,0) = \sum_{\mathbf{g}}\varphi_{\mathbf{g}}(x,y,0)\exp(2\pi i\mathbf{g}.\mathbf{r}) \tag{2.5}$$

and

$$\frac{\partial}{\partial z}\varphi_{\mathbf{g}}(\mathbf{r}) = 2\pi i s_{\mathbf{g}}\varphi_{\mathbf{g}}(\mathbf{r}) + \frac{i}{2k}\left[\frac{\partial^2}{\partial x^2} + \frac{\partial^2}{\partial y^2} + 2i(k_x + g_x)\frac{\partial}{\partial x} + 2i(k_y + g_y)\frac{\partial}{\partial y}\right]\varphi_{\mathbf{g}}(\mathbf{r}) + i\sigma\sum_{\mathbf{h}}u_{\mathbf{h}}(\mathbf{r})\varphi_{\mathbf{g}-\mathbf{h}}(\mathbf{r}), \tag{2.6}$$

where

$$s_{\mathbf{g}} = -(\pi/k_z)\,\mathbf{g}.[\mathbf{g} + \mathbf{k}/\pi]. \tag{2.7}$$

The condition imposed by equation (2.5) is compatible with the differential equation (2.6). It is now straightforward to show that the function $\psi(\mathbf{r})$ defined by

$$\psi(\mathbf{r}) = \sum_{\mathbf{g}}\varphi_{\mathbf{g}}(\mathbf{r})\exp(2\pi i\mathbf{g}.\mathbf{r}) \tag{2.8}$$

satisfies equation (2.1). Furthermore, by equation (2.5), $\psi(\mathbf{r})$ satisfies the boundary conditions at $z = 0$ and so $\psi(\mathbf{r})$ is the unique solution to Schrödinger's equation which satisfies the given boundary condition. Uniqueness can be seen by noting that if $\psi_1(\mathbf{r})$ and $\psi_2(\mathbf{r})$ are two solutions to equation (2.1) which satisfy the boundary condition, then $\psi'(\mathbf{r}) = \psi_1(\mathbf{r}) - \psi_2(\mathbf{r})$ also

satisfies the equation and the boundary condition, since $\psi'(x,y,0) = \psi_1(x,y,0) - \psi_2(x,y,0) = 0$. The solution to equation (2.1) when the incident wavefunction is zero is a function which is zero for all values of x and y and all positive values of z, *i.e.* $\psi'(\mathbf{r}) = 0$ and so $\psi_1(\mathbf{r}) = \psi_2(\mathbf{r})$ for all such values of $\mathbf{r}$. Hence, there is only one solution to equation (2.6) for given sets of functions $u_g(\mathbf{r})$ and $\varphi_g(x,y,0)$. Furthermore, for a different set of reciprocal lattice points, $\mathbf{h}$, and different functions $u_h(\mathbf{r})$ and $\varphi_h(x,y,0)$ representing the potential function $v(\mathbf{r})$ and the incident wavefunction $\psi(x,y,0)$, the solution $\varphi_h(\mathbf{r})$ to the equation corresponding to (2.6) represents the same scattered wavefunction as that represented by the functions $\varphi_g(\mathbf{r})$. $|\varphi_g(x,y,H)|^2$ is usually interpreted as the image formed by placing the objective aperture around the $\mathbf{g}$th reflection. It is shown in § 2.3 that this is not necessarily a proper interpretation if $\varphi_g(x,y,H)$ is a rapidly varying function of x and y.

2.2. *Reciprocal-space formulation of the scattering equations*

A useful form of equation (2.1) is obtained by taking its Fourier transform with respect to the variables x and y. If $\mathbf{u}$ is a two-dimensional vector in reciprocal space, then the Fourier transform of $f \equiv f(x,y)$ is defined as

$$\mathcal{F}_u(f) = \int \mathrm{d}x \int \mathrm{d}y f(x,y) \exp[-2\pi i(u_x x + u_y y)].$$

On using the convolution theorem for Fourier transforms one obtains from equation (2.1)

$$\frac{\mathrm{d}}{\mathrm{d}z} \Psi_u(z) = 2\pi i s_u \Psi_u(z) + i\sigma \int \mathrm{d}\mathbf{u}' V_{u'}(z) \Psi_{u-u'}(z), \quad (2.9)$$

where $\Psi_u(z)$ and $V_u(z)$ are the Fourier transforms of $\psi(\mathbf{r})$ and $v(\mathbf{r})$ respectively. s_u is defined by equation (2.7).

The use of equation (2.9) for image calculations by the method of periodic continuation (Grinton & Cowley, 1971) is discussed in § 3.2.

Equation (2.9) reduces to the standard set of scattering equations (Hirsch, Howie, Nicholson, Pashley & Whelan, 1965) if the crystal is perfect, in which case

$$V_u(z) = \sum_g V^{(g)} \delta(u_x - g_x)\, \delta(u_y - g_y) \exp(2\pi i g_z z),$$

$$\Psi_u(z) = \sum_g \Psi^{(g)} \delta(u_x - g_x)\, \delta(u_y - g_y) \exp(2\pi i g_z z),$$

where $\mathbf{g}$ is a three-dimensional lattice vector for the perfect crystal. On substitution of these expressions into equation (2.9), there result the standard equations

$$\frac{\mathrm{d}\Psi^{(g)}(z)}{\mathrm{d}z} = 2\pi i s_g \Psi^{(g)}(z) + \pi i \sum_h \xi_h^{-1} \Psi^{(g-h)}(z),$$

where $\xi_g = \pi/(\sigma V^{(g)})$ is the extinction distance for the gth reflection.

The effects of a finite objective aperture, spherical aberration and defocusing on the image can be readily calculated from $\Psi_u(z)$. If the objective aperture is centered on the point $\mathbf{u}_c$ and is of radius u_m in reciprocal space, it is appropriate to use the aperture function

$$A(\mathbf{u}) = 1 \quad |\mathbf{u}| < u_m$$
$$= 0 \quad |\mathbf{u}| \geq u_m.$$

With a defocus of ε and a coefficient of spherical aberration of C_s, the image intensity is found by considering the Fourier transform of

$$A(\mathbf{u}) \exp[\pi i \lambda \varepsilon (\mathbf{u} - \mathbf{u}_c)^2 + \tfrac{1}{2}\pi i C_s \lambda^3 |\mathbf{u} - \mathbf{u}_c|^4]\ \Psi_u(H). \quad (2.10)$$

2.3. *Conditions for interpreting $|\varphi_g(\mathbf{r})|^2$ as an image*

Howie & Basinski (1968) interpret $|\varphi_g(\mathbf{r})|^2$, obtained by solving equation (2.6), as the image which results from placing an aperture around the Bragg reflection $\mathbf{g}$. We now discuss the conditions under which such an interpretation is justified.

For this purpose it is convenient to carry out the analysis in reciprocal space. For $z = H$, the intensity at the point $\mathbf{g} + \mathbf{u}$ of the diffraction pattern is $|\Psi_{g+u}(H)|^2$ and may be obtained directly by solving equation (2.9) or by Fourier transformation of equation (2.8), in which case

$$\Psi_{g+u}(H) = \sum_h \Phi^{(h)}_{g-h+u}(H), \quad (2.11)$$

where $\Phi_u^{(h)}(z)$ is the Fourier transform of $\varphi_h(\mathbf{r})$. This equation expresses the intensity of diffracted electrons in terms of contributions from each of the functions $\varphi_g(\mathbf{r})$. As discussed in the previous section, the image that results when an objective aperture is centred on the reciprocal lattice point $\mathbf{g}$ is obtained by multiplication of equation (2.11) by the aperture function $A(\mathbf{u})$. Assuming that the objective aperture admits only one Bragg reflection, we distinguish three cases which are represented in Fig. 1.

(1) The only Fourier components of $\psi(x,y,H)$ which are admitted by the objective aperture are all of those of

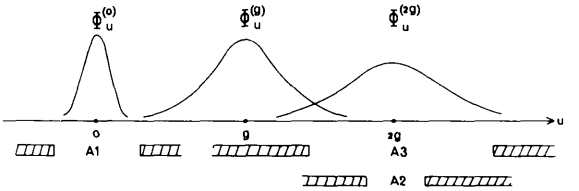

Fig. 1. Schematic representation of distribution of scattering from a non-periodic object. An image formed with (*a*) aperture $A1$ is given by $|\varphi_0(x)|^2$, (*b*) aperture $A2$ by $|\varphi_{2g}(x) * A2(x)|^2$, (*c*) aperture $A3$ by $|[\varphi_{2g}(x) + \varphi_g(x)\exp(-2\pi i g x)] * A3(x)|^2$. $\varphi_g(x)$ is the Fourier transform of $\varphi_u^{(g)}$ and $A2(x)$ denotes an aperture function in direct space.

$\varphi_g(x,y,H)$. This is the situation depicted in Fig. 1 when aperture $A1$ is used. The in-focus unaberrated image is given by

$$I(x,y) = |\int \mathrm{d}\mathbf{u}\, \Psi_u(H)\, A(\mathbf{u}-\mathbf{g}) \exp[2\pi i(\mathbf{u}-\mathbf{g}).\mathbf{r}]|^2$$
$$= |\int \mathrm{d}\mathbf{u}\, \Phi_u^{(g)}(H) \exp(2\pi i \mathbf{u}.\mathbf{r})|^2$$
$$= |\varphi_g(x,y,H)|^2, \qquad (2.12)$$

which is the interpretation usually given to the function $\varphi_g(\mathbf{r})$.

(2) Only some of the Fourier components of $\varphi_g(x,y,H)$ form the image (*e.g.* when aperture $A2$ of Fig. 1 is used). In this case, the image intensity is again given by the first line of equation (2.12) which reduces to

$$I(x,y) = |\int \mathrm{d}x' \int \mathrm{d}y'\, a(x-x', y-y')\, \varphi_g(x',y',H)|^2$$
$$\equiv |a(x,y) * \varphi_g(x,y,H)|^2,$$

where $a(x,y)$ is the Fourier transform of the aperture function $A(\mathbf{u})$.

(3) Fourier components of more than one of the functions $\varphi_g(x,y,H)$ contribute to the image (*e.g.* aperture $A3$ in Fig. 1). Then the image intensity is

$$I(x,y) = |a(x,y) * \sum_{\mathbf{h}} \varphi_{\mathbf{h}}(x,y,H) \exp[2\pi i(\mathbf{h}-\mathbf{g}).\mathbf{r}]|^2,$$

where the sum is over those values of $\mathbf{h}$ for which $\varphi_{\mathbf{h}}(x,y,H)$ makes a significant contribution to the image. Thus, whether the usual interpretation of the function $\varphi_g(\mathbf{r})$ is valid depends on the size of the objective aperture and on the extent of diffuse scattering around each Bragg reflection, or equivalently, on how rapidly the functions $\varphi_g(\mathbf{r})$ vary with x and y.

An indication of when the extent of diffuse scattering may be too great for equation (2.12) to be valid is obtained by considering the Fourier transform of equation (2.6)

$$\frac{\mathrm{d}}{\mathrm{d}z} \Phi_u^{(g)}(z) = 2\pi i s_{g+u} \Phi_u^{(g)}(z) + i\sigma \sum_{\mathbf{h}} \int \mathrm{d}\mathbf{u}'\, U_{u'}^{(h)}(z)$$
$$\times\, \Phi_{u-u'}^{(g-h)}(z), \qquad (2.13)$$

where $U_u^{(h)}(z)$ is the Fourier transform of $u_{\mathbf{h}}(z)$ with respect to x and y. In general the effect of the convolution integral in this equation is that the range of values of $\mathbf{u}$ for which $\Phi_u^{(g)}(z)$ is non-zero increases with depth in the crystal. This range depends on the range of values of $\mathbf{u}$ for which the function $U_u^{(g)}(z)$ is non-zero, *i.e.* on the amount of distortion of the crystal lattice perpendicular to the direction of the incident beam, and on the depth over which this distortion is significant. Thus, if the crystal is highly distorted, but only for a thin region, the ranges of values of $\mathbf{u}$ for which $\Phi_u^{(g)}(z)$ and $U_u^{(g)}(z)$ are significantly different from zero are approximately the same and the diffraction pattern at a particular point in reciprocal space results from only one of the functions $\varphi_g(\mathbf{r})$.

2.4. *Approximations*

The approximations to the direct-space equations (2.6) due to Takagi (1962) and Jouffrey & Taupin (1967) and the column approximation have already been mentioned. The former approximation consists in assuming that the second derivatives of the wave-functions $\varphi_g(\mathbf{r})$ are negligible, while the column approximation makes the additional assumption that the first derivatives with respect to x and y are negligible. The form of these approximations in the reciprocal space formulation of the scattering equation can be seen by considering equation (2.13).

The approximation of Takagi (1962) and Jouffrey & Taupin (1967) is to assume

$$s_{g+u}\, \Phi_u^{(g)}(z) = [s_g - (\pi/k_z)\, \mathbf{u}.(\mathbf{g} + \mathbf{k}/\pi)]\, \Phi_u^{(g)}(z) \quad (2.14)$$

in equation (2.13). The approximation assumes that terms involving $\lambda u^2\, \Phi_u^{(g)}(z)$ are negligible. The column approximation is

$$s_{g+u}\, \Phi_u^{(g)}(z) = s_g\, \Phi_u^{(g)}(z). \qquad (2.15)$$

In geometrical terms, the approximation of equation (2.14) corresponds to the replacement of the Ewald sphere in the regions around $\mathbf{g}$ by a plane tangential to the sphere, while equation (2.15) corresponds to approximating the sphere by a plane parallel to the $u_x - u_y$ plane. These approximations are indicated in Fig. 2. Note that a point on the Ewald sphere is not replaced by a unique point if the diffuse scattering contains contributions from more than one of the functions $\Phi_u^{(g)}(z)$. There is a different planar approximation for each of these functions.

An indication of the effects and importance of neglecting the term $(\pi/k_z)\, u^2\, \Phi_u^{(g)}(z)$ in equation (2.13) may be obtained by comparing an in-focus image with one that is out of focus by an amount equal to the thick-

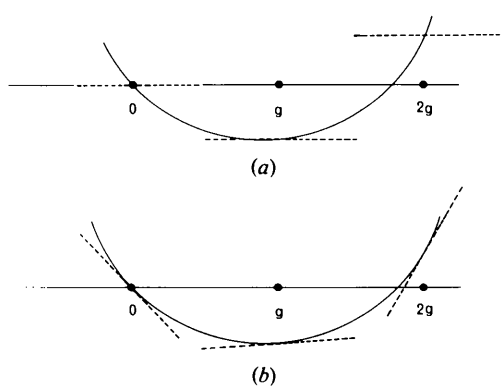

Fig. 2. Schematic representation of the Ewald sphere (full line) and approximations to it (broken line), (*a*) under the column approximation, (*b*) under the approximation of Takagi (1962) and Jouffrey & Taupin (1967).

ness of the crystal. If there are significant differences between the images at the resolution of interest it may be concluded that the term involving u^2 in equation (2.13) is significant and that the approximation of Takagi (1962) and Jouffrey & Taupin (1967) is unsatisfactory.

The above analysis indicates that whether or not the column approximation and the approximation of Takagi (1962) and Jouffrey & Taupin (1967) are valid depends upon the extent in reciprocal space of diffuse scattering around the Bragg reflections because the approximations of equations (2.14) and (2.15) become more accurate for decreasing $|\mathbf{u}|$. At the same time, it is evident from equation (2.13) that errors due to these approximations decrease with decreasing foil thickness so that, for any given level of resolution, the column approximations will be valid for a sufficiently thin crystal.

Approximations which treat scattering by a defect only to first order in the potential have been developed by Wilkens (1966, 1970) and Howie & Basinski (1968). Wilkens has applied the approximation to the calculation of images of small loops in thick foils. However, such approximations are often inappropriate at high resolution even for defects in thin foils. This is brought out in the work of Fields & Cowley (1978) who calculated scattering by interstitials in gold. Their calculations show that for a foil 20 Å thick, the diffraction pattern is significantly different from the predictions of the kinematic theory.

An approximation described by Spence (1978) is also correct only to first order in the potential functions of the defect. This approximation includes the effect of scattering from Bragg directions to directions of diffuse scattering but not the inverse scattering. This is similar to the assumption leading to the kinematic theory for a perfect crystal, a theory which is correct to first order in the potential.

Spence (1978) formulates the approximation in reciprocal space. The corresponding approximation in direct space is obtained by writing the potential function as $v(\mathbf{r}) = v^{(p)}(\mathbf{r}) + v^{(d)}(\mathbf{r})$ and the wavefunction as $\psi(\mathbf{r}) = \psi^{(p)}(\mathbf{r}) + \psi^{(d)}(\mathbf{r})$ (where $v^{(p)}(\mathbf{r})$ and $\psi^{(p)}(\mathbf{r})$ are periodic functions), and substituting these expressions into Schrödinger's equation (2.1). (For a pictorial representation, see Cowley, 1975, p. 143.) The approximation, which is to assume that the term $v^{(d)}(\mathbf{r})\,\psi^{(d)}(\mathbf{r})$ is negligible, will be valid if diffuse scattering by the non-periodic potential $v^{(d)}(\mathbf{r})$ is small.

In the high-voltage limit the approximation becomes

$$\frac{\partial}{\partial z}\psi^{(p)}(\mathbf{r}) = i\sigma v^{(p)}(\mathbf{r})\,\psi^{(p)}(\mathbf{r}),$$

$$\frac{\partial}{\partial z}\psi^{(d)}(\mathbf{r}) = i\sigma[v^{(p)}(\mathbf{r})\,\psi^{(d)}(\mathbf{r}) + v^{(d)}(\mathbf{r})\,\psi^{(p)}(\mathbf{r})],$$

from which the approximate wavefunction is found to be

$$\psi(x,y,H) = 1 + i\sigma\int_0^H \mathrm{d}z'\, v^{(d)}(x,y,z') \times \exp\left[i\sigma\int_0^H \mathrm{d}z'\, v^{(p)}(x,y,z')\right].$$

This example clearly brings out the first-order nature of the approximation.

3. Computation of images of defects

3.1. *Computations in direct space*

In principle, equation (2.1) (the form of Schrödinger's equation which neglects back-scattering) can be used in numerical work, but because the wavefunction $\psi(\mathbf{r})$ is a rapidly varying function of x and y, lengthy calculations would appear to be necessary for all but the thinnest crystals to account accurately for the terms involving the second derivative. Use of equation (2.6) is preferable because the $\varphi_g(\mathbf{r})$ are slowly varying functions of position compared with the $\psi(\mathbf{r})$, but even then there are situations in which a large part of a computation is taken up with evaluating the second derivatives of the wave function.

Several authors have computed images using equation (2.6) (Howie & Basinski, 1968; Howie & Sworn, 1970; Humphreys & Drummond, 1976), with the second derivatives being determined by comparison of $\varphi_g(\mathbf{r})$ at neighboring points. However, the computational necessity to limit the extent of this region means that the derivatives can be evaluated only approximately at the boundaries of the region. Computations have shown that care must be exercised to ensure that the effects of this approximation do not dominate the image. Distortion of the image may also occur if the distance between columns is too large (in certain cases, greater than 2 Å).

While equation (2.6) places no restriction on the form of the potential, it is most easily integrated when the functions $u_h(\mathbf{r})$ are slowly varying with position. For this reason computations based on the deformable-ion approximation are preferable to those using the rigid-ion approximation, since in the latter case the functions $u_h(\mathbf{r})$, if defined as in § 2.1, vary over a distance which is of the order of the periodicity of its highest-order Fourier component. Such variations can lead to difficulties for accurate numerical calculations involving the second derivative of the wavefunction. However, as an approximation, the deformable-ion model is less satisfactory for regions of large lattice displacements.

3.2. *Computations in reciprocal space*

Before one can use equation (2.9) in computations involving a defect, it is necessary to approximate the

integral by a summation. A suitable approximation is one used by Grinton & Cowley (1971), and further discussed by Cowley (1975) and Fields & Cowley (1978), in which a periodic structure is constructed from a finite region containing the defect. This structure then possesses an infinite array of defects although it does not necessarily correspond to a real crystal since, in general, no interaction between displacement fields of the defects is taken into account. The scattering is calculated as for a perfect crystal. There are a discrete set of Bragg beams, most of which correspond to the diffuse scattering due to a single defect. The distance in reciprocal space between Bragg reflections is inversely related to the periodicity of the structure and when the periodicity becomes infinitely large the calculation becomes one for a single defect. This method, the method of periodic extension or periodic continuation, has been used by Kuwabara & Uefuji (1975), MacLagan, Bursill & Spargo (1977), Spence (1978) and others to calculate images of defects. The structure factors of the periodic potential are of the form

$$\tilde{V}_{\mathbf{u}}(z) = \sum_{\mathbf{g}} V_{\mathbf{g}}\,\delta(\mathbf{u}-\mathbf{g}) + (MNab)^{-1}\sum_{m,n}\tilde{V}'_{\mathbf{u}}(z) \times \delta\left(u_x - \frac{m}{Ma}\right)\delta\left(u_y - \frac{n}{Nb}\right), \qquad (3.1)$$

where Ma and Nb are the periodicities in the x and y directions of the potential and are integral multiples of the periodicities (a,b) of the undeformed lattice. When this expression is substituted into equation (2.9), the convolution integral is reduced to a discrete summation and further, since the scattered wavefunction has the periodicity of the potential, its Fourier transform need only be evaluated at a discrete set of points in reciprocal space. Thus by constructing a periodic potential the problem is transformed into a form suitable for numerical work.

The structure factors calculated from a potential function describing an isolated defect are of the form

$$V_{\mathbf{u}}(z) = \sum_{\mathbf{g}} V_{\mathbf{g}}\,\delta(\mathbf{u}-\mathbf{g}) + V'_{\mathbf{u}}(z). \qquad (3.2)$$

If the deformed crystal lattice corresponds to the undeformed lattice everywhere but in a finite region then the Fourier coefficients $\tilde{V}'_{\mathbf{u}}(z)$ and $V'_{\mathbf{u}}(z)$ in equations (3.1) and (3.2) are equal at the points $\mathbf{u} = (m/Ma, n/Nb)$. However, for a defect such as an edge dislocation, for which the deformed and undeformed lattices do not coincide everywhere except in a finite range, the constructed periodic potential deviates significantly from a perfect crystal near the boundary of the unit cell, and thus the Fourier coefficients differ. Throughout the range of $\mathbf{u}$, the diffraction pattern calculated by the method of periodic continuation also contains information on the boundary of the unit cell. As Spence (1978) has pointed out, it may be necessary to introduce a non-planar incident wave, the intensity of which falls to zero at the boundary of the unit cell, in order to calculate the diffraction pattern due to an isolated defect.

In choosing the size of the periodic lattice for computations, precautions need to be taken to ensure that the periodic boundaries do not influence features of interest in the calculation. For image calculations this can be done by centering the feature of interest in the middle of the periodic cell and testing whether a change in the size of the cell alters the image features significantly.

4. Comparison of approximations

In this section the regions of validity of the approximations introduced in § 2 are tested by computing illustrative high-resolution images of an edge dislocation. Lattice-fringe images and dark-field weak-beam images are calculated using the deformable-ion and rigid-ion models of the potentials by means of both the direct-space equations (2.6) and the reciprocal-space equations (2.9). Additionally, weak-beam images and lattice fringe images are calculated by means of the column approximation, and these images are compared with the results of calculations using the method of periodic continuation.

4.1. *Assumptions*

All calculations are systematic calculations for 100 kV electrons. For the case of copper and silicon the systematic row *hh*0 of Bragg reflections is considered, while for calculations involving germanium the *hhh* systematic row is considered. The edge dislocation has the form shown in Fig. 3. It can be considered as resulting from the removal of atoms on the semi-infinite planes $x = \pm\frac{1}{4}d_{110}$, $z > 0$. Elastic theory predicts that in

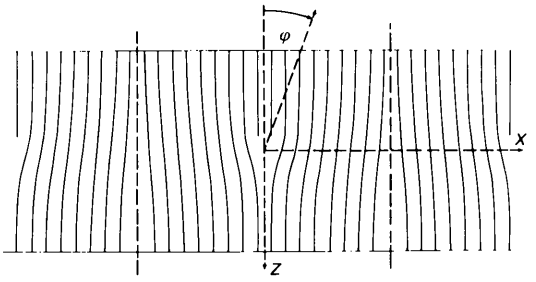

Fig. 3. Representation of an artificially periodic crystal, containing edge dislocations, which is used in the method of periodic continuation. The boundary of a unit cell is marked by the vertical broken lines. Note the 'defect' at the boundary.

the deformed lattice atoms at position (x,z) in the perfect crystal are displaced by

$$\mathbf{R}(x,z) = -\frac{\mathbf{b}}{2\pi}\left[\varphi - \frac{1}{4(1-\nu)}\sin 2\varphi\right], \quad -\pi < \varphi < \pi, \tag{4.1}$$

in the direction of the Burgers vector **b**. x, z and φ are defined in Fig. 3 and ν is Poisson's ratio which is taken to be $\frac{1}{3}$. A small displacement perpendicular to this displacement has not been considered in these calculations (Hirsch *et al.*, 1965).

4.2. *Rigid- and deformable-ion models*

As outlined in § 2.1, the rigid-ion model determines the potential at any given point in a deformed lattice by adding the potentials due to atoms individually positioned in the deformed lattice. The deformable-ion model determines the potential at any given point in the deformed lattice by equating it to the potential at some point in the perfect lattice. From this it is to be expected from the magnitude of the displacement field associated with the edge dislocation and the sizes of the unit cells being considered (Cu,Si,Ge) that the deformable-ion model will be adequate except possibly in the regions where the half-planes terminate. In this region the deformed potential may exceed the limits of the potential of the perfect lattice, and this cannot be described by the deformable-ion model. It is therefore of interest to see in which regions the models differ because of the implications for the interpretation of high-resolution images.

With the dislocation line parallel to the foil plane and x parallel to **b** (Fig. 3), structure factors of copper were calculated using the deformable-ion model for particular values of z by means of the equation

$$V_h^{(s)}(z) = V_g \int_{-md}^{md} \mathrm{d}x \exp(-2\pi i h x) \exp[2\pi i g R(x,z)],$$

$$h = \left(0, \pm\frac{1}{m}, \ldots, \pm 1\right)/2d, \tag{4.2}$$

where $d = d_{110}$, V_g is the structure factor corresponding to the reflection $gg0$ and $2md$ is the cell size. The results for copper for $m = 20$ for the 220 and 660 reflections are shown in Fig. 4. For the rigid-ion model, structure factors were calculated for an artificially periodic potential of periodicity $40d$. The atomic model is of the form indicated in Fig. 3. (A notable feature of the model is the presence of a defect midway between the edge dislocations. Structure factors calculated by means of such a model of the potential will differ from those for a single isolated defect in that the structure factor of the boundary defect (a 'hole') will be included.) When the contribution of the boundary defect is allowed for, structure factors around non-zero values of g calculated by the deformable-ion model and the rigid model agree to within 2% of the value of V_g. Structure factors around $g = 0$ are zero when calculated by the deformable-ion model. Calculations using the rigid-ion model show that for a distance greater than 8 Å in the z direction, structure factors around $g = 0$ are small.

Calculations show that for $z = 100$ Å the structure factors are close to those for a perfect crystal. As z decreases in magnitude, *i.e.* for regions close to the dislocation core, a number of structure factors in addition to those at reciprocal lattice points of the perfect crystal become significant. For some values of z they may become larger than that for the Bragg beam. For such regions a kinematic treatment of diffuse scattering may be inadequate for calculating the image intensity.

Comparing the structure factors around $\mathbf{g} = 220$ with those around $\mathbf{g} = 660$, it is seen that diffuse scattering is spread out more around higher-order Bragg reflections, which is to be expected on consideration of equation (2.4). This suggests that the column approximation will be less satisfactory when high-order reflections significantly influence the image.

4.3. *Dark-field weak-beam images*

Dark-field weak-beam images of an edge dislocation in copper with the geometry described in § 4.1 were calculated using a number of different approximations in order to determine their accuracy. The point of termination of the extra half-planes was taken as 50 Å below the entrance face of the crystal and values of the total crystal thickness up to 450 Å were considered. While these represent experimentally small values of

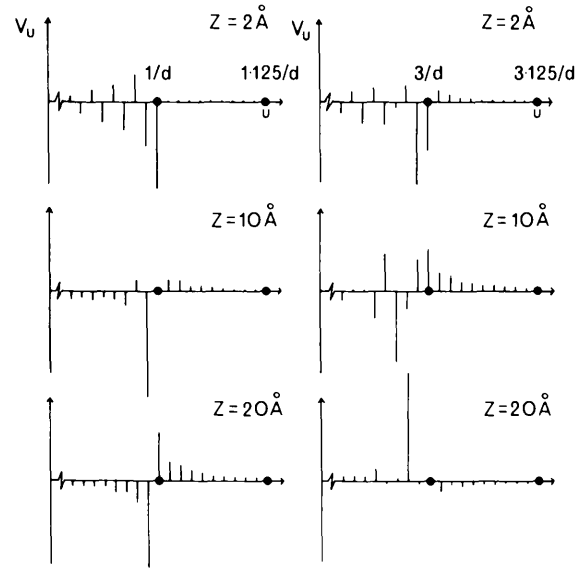

Fig. 4. Structure factors around reciprocal lattice points $g = 220$ and $g = 660$ calculated along lines at distance z from an edge dislocation in copper; $d = d_{220}$.

dislocation depth and foil thickness, they are adequate for purposes of comparing methods of calculating images. Calculations included the 000 and 220 reflections, *i.e.* calculations were 'two-beam', with the crystal oriented so that the Ewald sphere passed through the point $1/d$ (6·2, 6·2, 0). A slice thickness of 5 Å was used in the calculation and no absorption was included.

Images were calculated by means of:

(1) The reciprocal-space equation (2.9) and the rigid-ion model along with the method of periodic continuation. The image was formed by assuming an objective aperture radius of 0·4 $Å^{-1}$.

(2) The direct-space equation (2.6) with the rigid-ion model and the method of periodic continuation. The potential functions were defined as

$$u_0(x,z) = \sum_{j=-(N-1)}^{N-1} V_h(z) \exp(-2\pi i h x),$$

$$u_g(x,z) = \sum_{j=-N}^{N} V_{g+h}(z) \exp(-2\pi i h x),$$

where $h = j/Na$ and where $V_h(z)$ is the structure factor calculated from the artificially periodic potential of period Na. The image intensity was assumed to be equal to $|\varphi_g(x,z)|^2$.

(3) The assumptions described in (2) above along with the additional assumption of the column approximation.

(4) Equation (2.6) and the deformable-ion model. The choices of potential functions were

$$u_0(x,z) = V_0,$$

$$u_g(x,z) = V_g \exp[-2\pi i g R(x,z)],$$

and the image intensity was taken equal to $|\varphi_g(x,z)|^2$.

(5) The assumptions of (4) and the column approximation.

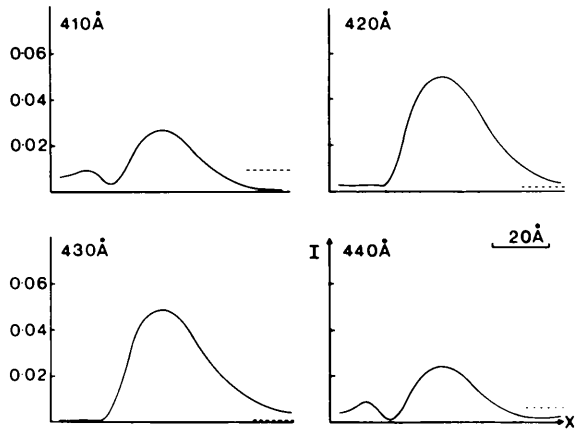

Fig. 5. Dark-field weak-beam images of an undissociated edge dislocation at a depth of 50 Å in copper foils of thickness ranging from 410 to 440 Å. The image is formed with the $g = 220$ reflection. The Burgers vector is $\mathbf{b} = a/2[110]$ and $s_g = 2 \times 10^{-2}$ $Å^{-1}$. The background intensity is indicated by the broken line.

For all calculations, images of the form shown in Fig. 5 were obtained. The shapes and heights of the weak-beam image peaks calculated by these five methods were not found to be significantly different at the 3 Å level of resolution. The periodic dependence of the height of the peak on the thickness of the crystal and the width of the peak were found to be consistent with a kinematic description of the scattering (Cockayne, 1972). Images at four different thicknesses are shown in Fig. 5. The small feature to the left of the peak which appears at some thicknesses is seen to be below the level of the background intensity indicated by a dotted line and so is not considered an observable feature (for a discussion, see Cockayne, 1978). The only significant effect of making the column approximation is to cause a miscalculation in the position of the image. This indicates that the term involving the second derivative of the wavefunction is not important and that neglect of the term $-(k_x/k)\,\partial\varphi_g(\mathbf{r})/\partial x$ in equation (2.6) means that a shift of the image relative to the position of the defect is not calculated. This shift is due to the fact that the Bragg beam which forms the weak-beam image is not in the direction of the z axis within the crystal.

The above calculations are based on a 'two-beam' approximation. To determine the effects of making this aproximation, equation (2.6) with the deformable-ion model was integrated taking into account four beams. A comparison of images calculated with and without the column approximation shows that, as for the two-beam calculation, they differ only in a slight displacement. This displacement is less than that in the two-beam case.

Howie & Sworn (1970), using equation (2.6), concluded that the column approximation results in significant distortion of the weak-beam image formed with the 440 reflection when the 220 reflection is satisfied. Our calculations using this equation give no evidence of the column approximation producing distortion of the 440 image. However, distortion similar to that calculated by Howie & Sworn occurs if the distance between columns is taken as 4 Å. It disappears if the distance is chosen as 2 Å or less. Further spurious effects arise if the boundary of the region of calculation is less than 20 Å from the part of the image which is of interest. From our calculations we conclude that in this case too the column approximation results only in a displacement of the image.

4.4. *Lattice-fringe images*

We now consider the applicability of the column approximation for calculating lattice-fringe images near an edge dislocation in a crystal of silicon which is viewed along the dislocation line direction (*i.e.* for the displacement field shown in Fig. 3, the foil normal is parallel to the y axis, with the x axis parallel to [110]).

Systematic calculations were made of an image along a line $z = 0$ defined in Fig. 3. The model of the potential is one in which there are four atoms at each of the positions

$$x_{k+n} = \pm(\tfrac{1}{2}na + 5ka), \quad n = 1, 2, \ldots, 9, \quad k = 0, 1, 2, \ldots,$$

i.e. the potential is periodic and atoms are on the points of a lattice except at points $\pm 5ka$. The structure factors for such a structure can be regarded as being those for a perfect crystal less four times the form factor for a single atom of silicon. This is shown in Fig. 6.

Since the structure factors are significantly different from zero midway between reciprocal lattice points it is to be expected that the predictions with the column approximation will not be accurate (see § 2.5), and this is seen in the following analysis.

We consider the orientation in which the 220 reflection is satisfied and images are formed by centering the objective aperture midway between the incident beam and this Bragg beam, both of which contribute to the image. Two-beam calculations were performed for thicknesses up to 240 Å. The potential was considered to be independent of depth in the crystal.

Two sets of images, shown in Fig. 7, were calculated, one by integrating equation (2.6) under the assumption of the column approximation, and the other by integrating equation (2.9) by the method of periodic continuation. Since the deformable-ion model is inappropriate for describing the potential near the core of the dislocation, the functions $u_0(x)$ and $u_g(x)$ in equation (2.6) were defined by

$$u_0(x) = \sum_{j=-5}^{4} V_h \exp(-2\pi ihx),$$

$$u_g(x) = \sum_{j=-5}^{5} V_{h+g} \exp(-2\pi ihx),$$

where $h = j/5a$. The image intensity, for those calculations based on the column approximation, is given by $|\varphi_0(x,H) + \varphi_g(x,H)\exp(2\pi igx)|^2$. The calculations using the method of periodic continuation take into account reflections from $j = -5$ to $j = +15$. All of these reflections were used to form the lattice fringe images.

Images at different thicknesses are shown in Fig. 7. At a thickness of 40 Å, images calculated by the two methods are very similar. This is to be expected since the effect of Fresnel diffraction, which is treated only approximately by the column approximation, is small. For thicker crystals significant differences between the two sets of images are apparent because Fresnel diffraction effects increase with increasing thickness. At 240 Å thickness, the images calculated using the method of periodic continuation show a spacing of fringes near the core of the dislocation which differs from the spacing of the lattice planes. In comparing this image with the image from a thin crystal, an additional fringe appears to the left of the core and the first fringe on the left is displaced approximately 0·4 Å, or 20% of the fringe spacing. Such a distortion of fringe spacings

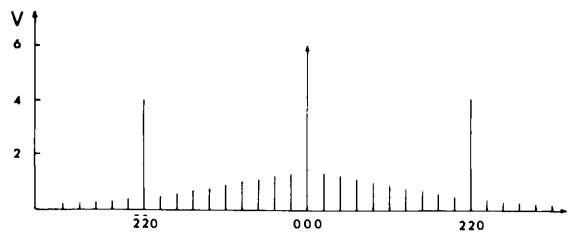

Fig. 6. Structure factors for an edge dislocation in silicon calculated by considering atoms along the line $z = 0$ (defined in Fig. 3) and using an artificial potential with length of unit cell ten times that of the perfect crystal.

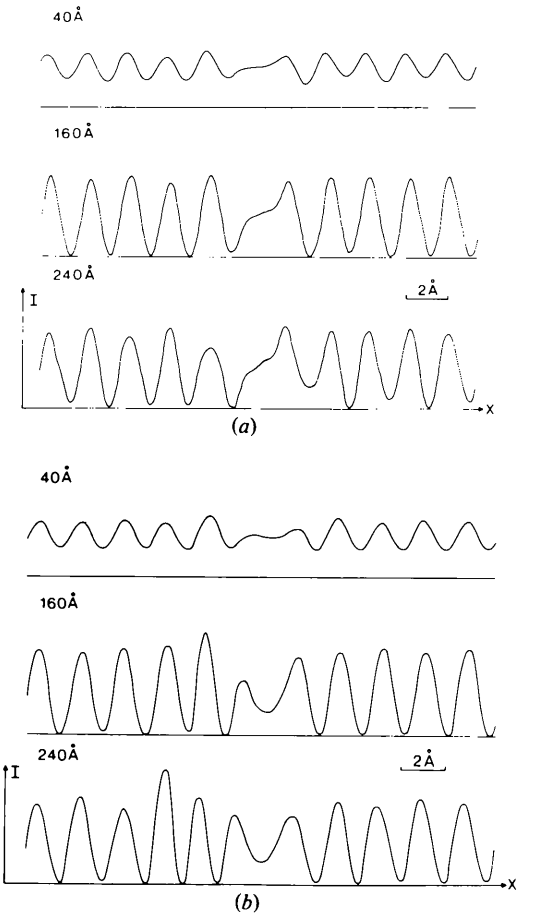

Fig. 7. (220) lattice fringes along the line $z = 0$ of an edge dislocation in silicon viewed along the dislocation line. Fringes from foils of varying thickness are calculated (*a*) by means of the column approximation and (*b*) using equation (2.9). The crystal is oriented so that $s_{220} = 0$.

appears to have been observed experimentally in aluminium by Parsons & Hoelke (1969). That this distortion is not due to the boundary of the unit cell was verified by calculating with an artificial unit cell of 20 times the length of the basic unit cell.

The image calculations of § 4.3 and § 4.4 illustrate the conclusions that the column approximation cannot be assigned an absolute resolution limit of validity. Rather, whether or not it can be used in a particular case is determined by the effects of Fresnel diffraction, which depend upon foil thickness, electron wavelength and, above all, the extent of diffuse scattering in the region between Bragg reflections. On the other hand, calculations show that for the case considered in § 4.3, the kinematic theory (even when it treats wave propagation exactly) is inadequate for calculating images even for a foil thickness of 40 Å.

5. Interpretation of high-resolution images

In this section, the method of periodic continuation is used to study two experimental methods currently under consideration for investigating dislocation cores, *viz* the lattice-fringe method and the weak-beam method. Both of these methods aim to obtain electron microscope images which can be interpreted in terms of dislocation structures. The restrictions on making a direct interpretation are investigated below.

5.1. *Lattice fringe images in germanium*

With the geometry described in § 4.1, (111) lattice-fringe images were calculated along a line parallel to [110] through the core of a sessile edge dislocation in germanium which was viewed in the direction $[1\bar{1}0]$ along its line. This geometry was chosen to correspond with the experiment of Bourret, Desseaux & Renault (1977). The lattice spacing is $d_{111} = 3{\cdot}27$ Å, a spacing suitable for resolution by a modern electron microscope operating at 100 kV when the foil is oriented so that the 111 and $\bar{1}\bar{1}\bar{1}$ reflections are equally distant from the Ewald sphere.

Images were calculated by the method of periodic continuation for foil thicknesses up to 320 Å. A unit-cell size of $20d_{111}$ was used and reflections from $\bar{2}\bar{2}\bar{2}$ to 222 were included in the calculation. Images for a range of thicknesses are shown in Fig. 8. The objective aperture admits all reflections within $1{\cdot}3/d_{111}$ Å^{-1} of the origin. At 40 Å thickness, the spacing of fringes equals the spacing of lattice planes. As the thickness of the foil increases, this correspondence fails to hold for fringes close to the core of the dislocation.

Spence, O'Keefe & Kolar (1977) have calculated two-dimensional lattice images of a perfect crystal of germanium. They show that images which correspond directly with the structure of the crystal exist in thicker regions of a foil as well as in thin foils. These thicknesses can be predicted from a consideration of the thickness dependence of the amplitudes and phases of diffracted beams. Calculations for a perfect crystal in the orientation considered here predict that images at 40 and 320 Å thickness should correspond in perfect regions of the crystal. An examination of the images at these thicknesses in Fig. 8 show that away from the dislocation core the positions of lattice fringes are very close for the two thicknesses, but close to the dislocation core the separation of fringes differs by as much as 5% in the thicker foil. Thus it may be concluded that there may not be a direct correspondence between images and structures of defects for a particular foil thickness even if, for that thickness, the relationship in the perfect crystal is a direct one. This is in agreement with the conclusions of Spence, O'Keefe & Iijima (1979) based on two-dimensional calculations.

These results suggest that to investigate structure it is easiest to examine thin foils. However, spherical aberration of the objective lens may distort the image even of a thin crystal. Fig. 9 shows images calculated for a 40 Å foil when the coefficient of spherical aberration is 0·7 mm for a range of defocus values around an optimum value of 900 Å underfocus using equation (2.10). The radius of the objective aperture is $1{\cdot}3/d_{111}$ Å^{-1}. In these examples, spherical aberration causes a distortion of up to 5% in the spacing of fringes compared with the spacing of lattice planes. Calculations show that the distortion depends on the radius of the objective aperture. Thus even for a thin crystal

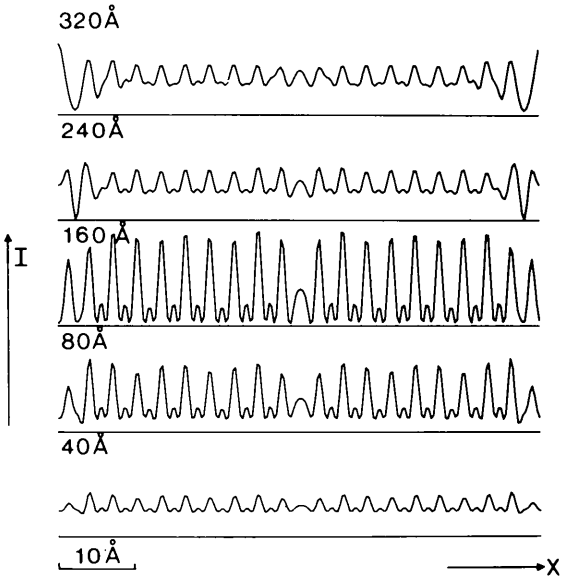

Fig. 8. (111) lattice fringes along a line parallel to [110] through the core of a sessile edge dislocation in germanium viewed along its line for foils of various thickness. The foil is oriented so that $s_{111} = s_{\bar{1}\bar{1}\bar{1}}$.

there may not be a direct relationship between image and structure of a distorted region of the crystal.

Bourret, Desseaux & Renault (1977) have compared the position of experimental lattice-fringe images near an edge dislocation in a thin foil of germanium with the position of lattice planes calculated by elastic theory of dislocations. Close to the dislocation, differences between the fringes and calculated lattice planes are evident. Two-dimensional calculations are needed to determine to what extent the difference is due to the inadequacy of the model and how much is due to instrumental parameters.

From the calculations of this section and those of § 4.4, the following points can be made.

(1) Near an edge dislocation the effects of Fresnel diffraction can cause distortion in lattice-fringe spacings in thick foils, both when the Bragg condition is satisfied and when a symmetric orientation is employed. Distortion may also occur near the dislocation at those foil thicknesses for which there is a direct relationship between structure and image for the perfect crystal.

(2) Spherical aberration and the amount of defocus of the objective lens may cause distortion of the image near the centre of the dislocation even for thin foils. The amount of distortion depends on the radius of the objective aperture.

5.2. *High-resolution weak-beam images*

The possibility of using dark-field weak-beam images to study the structure of dislocation cores has been suggested by the results of earlier image calculations (Cockayne & Vitek, 1974). In these earlier studies, two dislocation core models were used, one based on a singular Volterra-type dislocation (hereafter referred to as a singular core) and one based on atomic positions determined from atomistic calculations with a particular atomic potential (extended core). Weak-beam images were calculated for these core models, and it was demonstrated that extended cores showed image detail at the 5 Å level of resolution which was not present in images calculated for singular cores. The most significant feature of the images was a 'core peak' in the case of the extended-core model, identified as a narrow (approximately 5 Å width at half-height) region of intensity many times background. An example is shown in Fig. 10, and the core peak is found repeatedly in weak-beam images calculated for dislocations at various depths and in foils of differing thickness, when the dislocation has an extended core. Consequently it was suggested that such image detail might offer a means of studying the core.

The scattering equations used to calculate the image shown in Fig. 10 make use of the column approximation, and it is necessary to establish that this approximation is reliable at the resolution involved in detecting the core peak in Fig. 10. For this reason, images were calculated using equation (2.9) and the method of periodic extension discussed previously in this paper.

Calculations have been performed for the defect geometry shown in Fig. 3. From this figure it is apparent that, as well as the defect of interest in the centre of the extended cell, there is an 'additional' defect at the boundary caused by the termination of the extended cell in an imperfect crystal. The influence of this additional defect at the boundary upon the diffraction pattern and image has been discussed in §3.2.

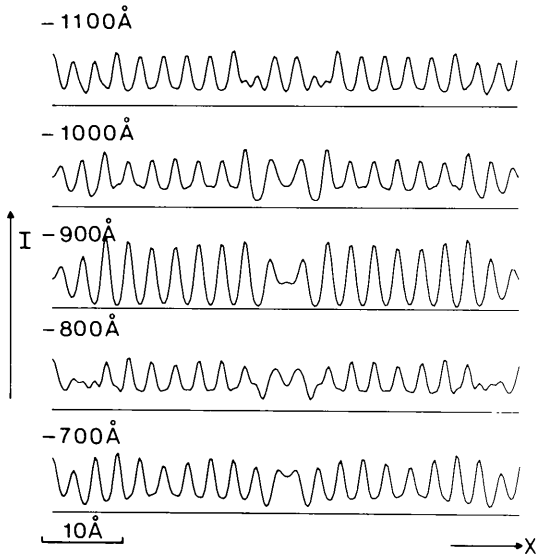

Fig. 9. (111) lattice fringes in germanium for a foil thickness of 40 Å, C_s = 0·7 mm and varying values of defocus of the objective lens. Other details as for Fig. 8.

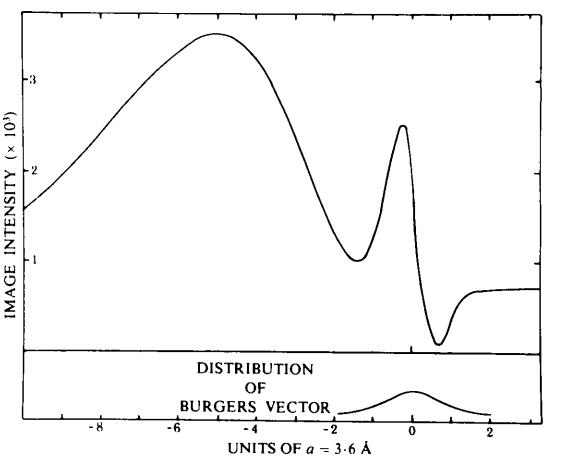

Fig. 10. Weak-beam image calculated with the column approximation for an undissociated edge dislocation in copper, but with an extended core (for core parameters see Vitek & Cockayne, 1974). Dislocation depth = 1·54ξ_g, foil thickness = 3·04ξ_g, g = 220, 100 kV electrons, six-beam calculation, $s_{220} = 2 \times 10^{-2}$ Å^{-1}.

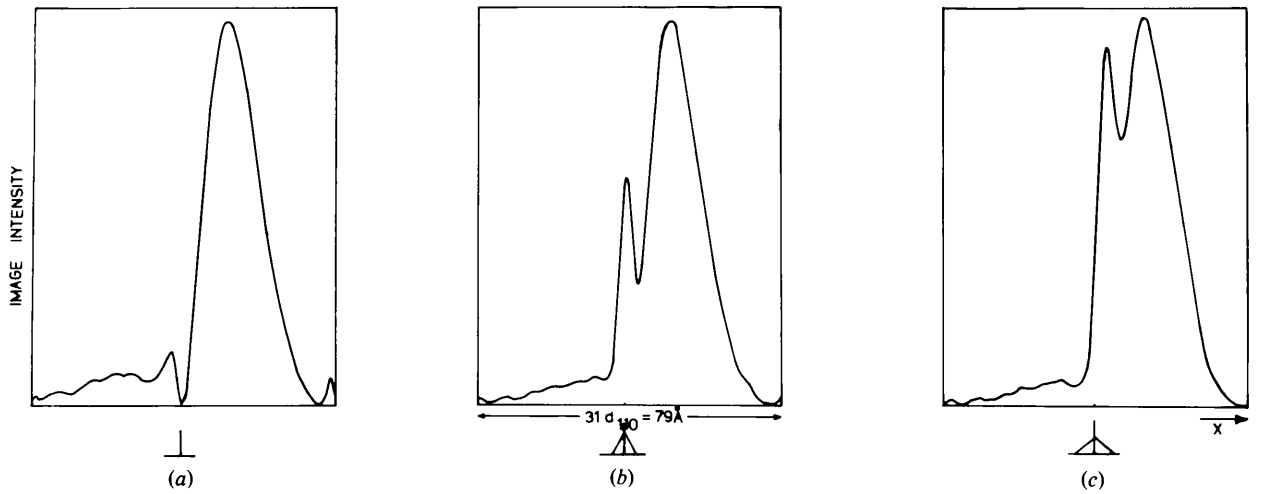

Fig. 11. Weak-beam images calculated with the method of periodic continuation for undissociated edge dislocations at a depth of 50 Å ($=0{\cdot}1\xi_g$) in a copper foil of thickness 140 Å. The diffraction geometry has $g = 220$ with $s_{220} = 2{\cdot}85 \times 10^{-2}$ Å^{-1} and 100 kV electrons. The core models are as for equation (5.1) with (*a*) $2X = 0$ Å, (*b*) $2X = 10$ Å, (*c*) $2X = 15$ Å. The sensitivity of the 'core peak' to the core 'width' $2X$ is to be noted.

Fig. 11(*a*) shows a calculated weak-beam image for a dislocation at depth 50 Å in copper for the diffraction geometry given. The image is obtained by allowing all elastic diffuse beams from $31g'$ to $93g'$ to contribute to the image, where $g' = 1/(62d_{220})$. Included in the calculation are reflections $-g'$ to $93g'$. The extended cell is 79 Å $= 62d_{220}$ wide. The image is very similar to those obtained using equation (2.6) with the column approximation, and there are no differences significant at the level of 5 Å. In particular, there is no evidence of any core peak in images calculated using the extended-cell method when singular core models of defects are used.

For many materials, the singular Volterra dislocation core is unsatisfactory when particular properties of dislocation (*e.g.* ease of cross-slip) are being considered. In a study of what influence core parameters have on dislocation dissociation, Cockayne & Vitek (1974) used a core model with atomic coordinates determined from atomistic calculations using a potential for copper. In this model, the core structure of the dislocation was described as a distribution of discrete closely spaced singular dislocations, the sum of whose Burgers vectors is equal to the Burgers vector of the total dislocation (for further details see Cockayne & Vitek, 1974). The distribution of the atoms in this 'extended' core compared with the distribution for a singular core is reflected in the variation of $\mathrm{d}R_x/\mathrm{d}z$ with x (where R_x is the atomic displacement along the slip plane in the direction x parallel to the Burgers vector, and z is the coordinate perpendicular to the slip plane). In Fig. 12 this variation, for planes at a distance $z = \pm d_{111}/2$ from the slip plane, is shown. For the extended core, a maximum value of $|\mathrm{d}R_x/\mathrm{d}z|$ occurs at a small distance from the center of the dislocation, while for the singular core the term is monotonically increasing.

In the present study, a simplified analytical model of the atomic displacements in the core region has been constructed with variable parameters which enable the influence of different core models upon the image to be studied. In this model, the atom at position x,z in the extended cell is displaced a distance $\mathbf{R}(x,z)$ as given by equation (4.1) for a dislocation with a singular core. However, atoms inside a 'core' of dimensions $2X$ by $2Z$ centered on the dislocation (see Fig. 10) are displaced by $\mathbf{R}'(x,z)$ where

$$\mathbf{R}'(x,z) = \mathbf{R}(2X - x, z) \quad \text{for } x > 0,$$
$$\mathbf{R}'(x,z) = \mathbf{R}(-2X - x, z) \quad \text{for } x < 0. \qquad (5.1)$$

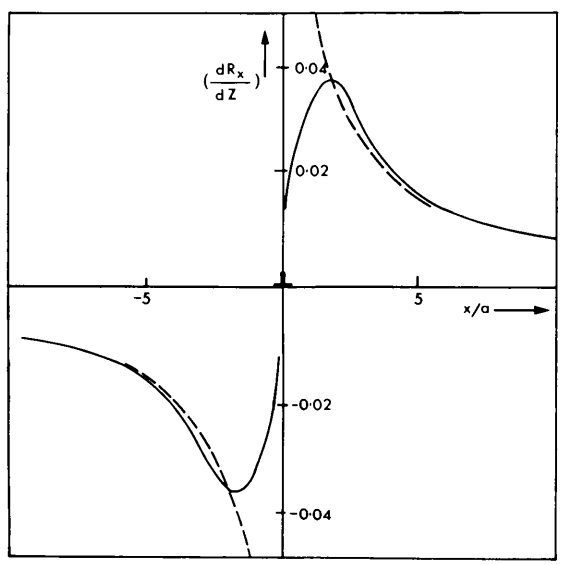

Fig. 12. The variation of $\mathrm{d}R_x/\mathrm{d}z$ with x for an undissociated edge dislocation, at a distance $z = \pm d_{111}/2$ from the slip plane. Curves for an extended (——) and singular (– – –) core are shown.

With this model, atom displacements have a mirror symmetry across the core boundaries at $x = \pm X$. Consequently, $|dR_x/dz|$ has a maximum value at $x = \pm X$, as shown in Fig. 12 for the core model of Cockayne & Vitek (1974) discussed previously.

Using the above dislocation model and the periodic continuation method of image computation, images were calculated for the same cell parameters and diffraction geometry as used for Fig. 11(*a*). Examples of the images obtained are shown in Fig. 11(*b*), (*c*). When compared with the images for the singular core shown in Fig. 11(*a*), the images of the extended core show an additional prominent 'core' peak. This result confirms the presence of core peaks in images of extended cores suggested by earlier column approximation calculations (Cockayne & Vitek, 1974).

It is of interest to determine where in the diffraction pattern the information concerning the core peak is to be found, if only to determine the size of objective aperture required to include the information in the image. By comparing intensities in the elastic diffuse beams for the singular and extended cores, it is evident that information concerning the core peak is concentrated in two side-bands around the Bragg position of the perfect crystal (see Fig. 13). The elastic diffuse reflections for the extended core show an increase in magnitude of up to six times that for the singular core. In this case, it is necessary to include this region of the diffraction pattern within the objective aperture to observe the core peak in the image, and this is demonstrated by computationally forming images using different extents of the diffraction pattern.

To determine whether a core peak might be associated with a singular dislocation through instrumental parameters, the effects of the radius of the objective aperture, spherical aberration and defocus were examined using the results of the scattering calculations from the equations in reciprocal space. For in-focus images, no significant differences in image detail were observed in changing the radius of the objective aperture from 0·05 Å^{-1} to higher values, or when the coefficient of spherical aberration was increased to 5 mm.

The effects of defocusing by several thousand ångströms are shown in Fig. 14. The radius of the objective aperture is 0·25 Å^{-1} and the spherical aberration is zero. Image detail was found not to be sensitive to small changes in these parameters. Following the discussion of § 2.4, these calculations suggest that approximating the second derivatives in equation (2.6) by zero is justified for an edge dislocation within one or two thousand ångströms of the exit face of the crystal. For thicker crystals any effects from this approximation are likely to be insignificant compared with the effects of convergence of the incident beam and thermal diffuse scattering.

It can be concluded that the column approximation and the deformable-ion model can adequately account for the features of a weak-beam image of an edge dislocation in the orientation considered here, and that the image intensity is given by $|\varphi_g(x)|^2$ provided that the image is approximately in focus. This conclusion means that any details which might be observed in experimental in-focus images which do not correspond to the single peak predicted by the simple model of the dislocation considered here, will require a different model of the dislocation.

6. Conclusions

From the forgoing analyses, the following conclusions can be drawn:

(1) The set of scattering equations considered by Howie & Basinski (1968) is valid irrespective of the

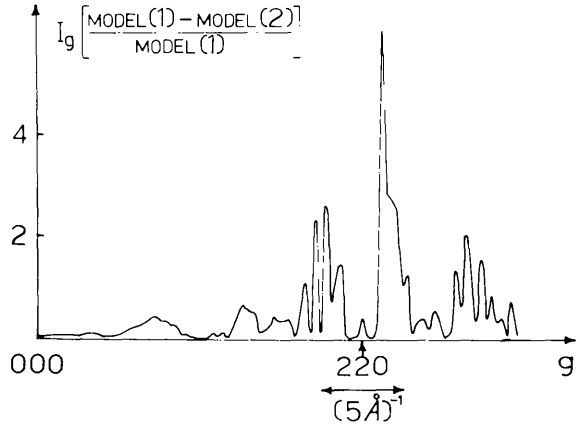

Fig. 13. Plot of relative diffracted intensities for crystals containing undissociated edge dislocations with core models (1) $2X = 15$ Å, (2) $2X = 10$ Å, according to equation (5.1). Parameters as for Fig. 11.

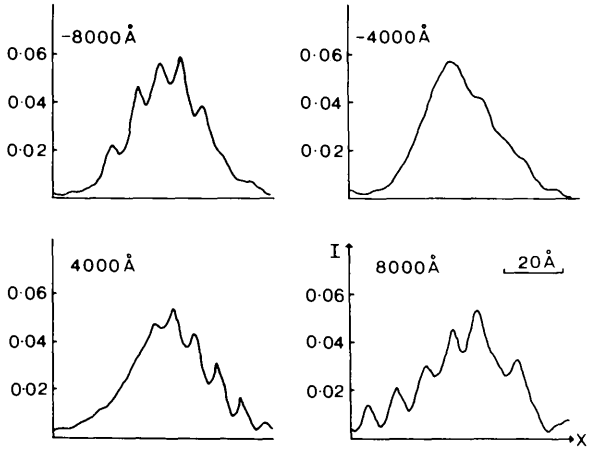

Fig. 14. Dark-field weak-beam images of a singular edge dislocation in copper for varying values of defocus. The radius of the objective aperture is 0·25 Å^{-1}. Other details as for Fig. 5.

degree of distortion of the crystal. However, to retain their usefulness in image computations when significant diffuse scattering exists between Bragg reflections, the effects of the objective aperture must be explicitly included in calculations of images using these equations, *i.e.* the effects of overlapping diffuse scattering must be included in image calculations.

(2) Whether or not the column approximation or the approximation of Takagi (1962) and Jouffrey & Taupin (1967) are valid depends upon the extent of diffuse scattering. For any given level of resolution and degree of distortion, the column approximation is valid for a sufficiently thin crystal.

(3) In general for numerical work, the equations of Howie & Basinski (1968) are easiest to integrate when the deformable-ion model and the approximation of Takagi (1962) and Jouffrey & Taupin (1967) are valid. The method of periodic continuation is best suited to calculations in which significant image-detail occurs only over a small region.

(4) Calculated weak-beam images of dislocations with extended cores show image peaks not present in calculated images of dislocations with singular cores.

(5) Because of spherical aberration and, in thick foils, Fresnel diffraction, there may not be a direct correspondence between lattice fringes and lattice planes near the core of a dislocation, even if the correspondence is a direct one in perfect regions of the crystal.

The support of a postdoctoral research fellowship (GRA) from the Australian Institute of Nuclear Science and Engineering is gratefully acknowledged, as is support from the Australian Research Grants Committee. The authors wish to thank K. Mason for assistance with computing and Dr J. C. H. Spence of Arizona State University for helpful comments.

References

BOURRET, A., DESSEAUX, J. & RENAULT, A. (1977). *J. Microsc. Spectrosc. Electrons*, **2**, 467–474.

COCKAYNE, D. J. H. (1972). *Z. Naturforsch. Teil A*, **27**, 452–460.

COCKAYNE, D. J. H. (1978). *Proc. 6th Eur. Reg. Conf. Electron Microsc., Jerusalem*, **1**, 109–111.

COCKAYNE, D. J. H. & VITEK, V. (1974). *Phys. Status Solidi B*, **65**, 751–764.

COWLEY, J. M. (1975). *Diffraction Physics*. Amsterdam: North-Holland.

FIELDS, P. M. & COWLEY, J. M. (1978). *Acta Cryst.* A**34**, 103–112.

GOODMAN, P. & MOODIE, A. F. (1974). *Acta Cryst.* A**30**, 280–289.

GRINTON, G. & COWLEY, J. M. (1971). *Optik (Stuttgart)*, **34**, 221–233.

HIRSCH, P. B., HOWIE, A., NICHOLSON, R. B., PASHLEY, D. W. & WHELAN, M. J. (1965). *Electron Microscopy of Thin Crystals*. London: Butterworths.

HIRSCH, P. B., HOWIE, A. & WHELAN, M. J. (1960). *Philos. Trans. R. Soc. London, Ser. A*, **252**, 499–529.

HOWIE, A. & BASINSKI, Z. S. (1968). *Philos. Mag.* **17**, 1039–1063.

HOWIE, A. & SWORN, C. H. (1970). *Philos. Mag.* **22**, 861–864.

HOWIE, A. & WHELAN, M. J. (1961). *Proc. R. Soc. London Ser. A*, **263**, 217–237.

HOWIE, A. & WHELAN, M. J. (1962). *Proc. R. Soc. London Ser. A*, **267**, 206–230.

HUMPHREYS, C. J. & DRUMMOND, R. A. (1976). *Proc. 6th Eur. Reg. Conf. Electron Microsc., Jerusalem*, **1**, 142–146.

JOUFFREY, B. & TAUPIN, D. (1967). *Philos. Mag.* **16**, 703–715.

KUWABARA, S. & UEFUJI, T. (1975). *J. Electron Microsc.* **24**, 137–144.

MACLAGAN, D. S., BURSILL, L. A. & SPARGO, A. E. (1977). *Philos. Mag.* **35**, 757–780.

PARSONS, J. R. & HOELKE, C. W. (1969). *J. Appl. Phys.* **40**, 866–872.

SPENCE, J. C. H. (1978). *Acta Cryst.* A**34**, 112–116.

SPENCE, J. C. H., O'KEEFE, M. A. & IIJIMA, S. (1979). *Philos. Mag.* In the press.

SPENCE, J. C. H., O'KEEFE, M. A. & KOLAR, H. (1977). *Optik (Stuttgart)*, **49**, 307–323.

TAKAGI, S. (1962). *Acta Cryst.* **15**, 1311–1312.

TOURNARIE, M. (1962). *J. Phys. Soc. Jpn*, **17**, *Supplement* B-II, 98–100.

WILKENS, M. (1966). *Phys. Status Solidi*, **13**, 529–542.

WILKENS, M. (1970). *Modern Diffraction and Imaging Techniques in Material Science*, edited by S. AMELINCKX, R. GEVERS, G. REMAUT & J. VAN LANDUYT, pp. 233–256. Amsterdam: North-Holland.